Lifshitz-enhanced superfluid density in two-gap superconducting TiSe2

npj | quantum materials

Article

Published in partnership with Nanjing University

https://doi.org/10.1038/s41535-025-00834-8

Lifshitz-enhanced superfluid density in two-gap superconducting $TiSe_2$

F. Elson[1] ✉, J. Philippe[2,3], G. Simutis[2,4], O. K. Forslund[3,5], M. Abdel-Hafiez[6], M. Janoschek[2,3], R. Khasanov[2], D. Das[2], J. Weissenrieder[1], D. W. Tam[1], Y. Sassa[1] ✉ & M. Månsson[1] ✉

Superconductivity in $TiSe_2$ emerges when the charge density wave (CDW) order is suppressed under pressure or doping. Recent theoretical and experimental studies suggest that a Lifshitz transition plays a key role in stabilizing the superconducting phase. Here, we present muon spin resonance measurements of pressurized $TiSe_2$, revealing a two-gap superconducting state. Our results indicate that the smaller gap contributes unexpectedly strongly to the total superfluid density. This effect is consistent with an enhanced density of states in a newly formed Fermi surface pocket at the Lifshitz transition. These findings provide microscopic insight into the interplay between CDW suppression, Fermi surface reconstruction, and multi-gap superconductivity in $TiSe_2$, demonstrating how pressure-induced changes in electronic structure can shape superconducting properties in layered materials.

Layered transition metal dichalcogenides (TMDs) host a rich interplay between charge order, superconductivity, and electronic correlations, making them a fertile ground for emerging quantum phenomena[1]. Among them, *1T*-$TiSe_2$ has attracted particular interest due to its unconventional charge density wave (CDW) phase, which competes with superconductivity under pressure or chemical doping[2,3]. *1T*-$TiSe_2$ adopts a hexagonal layered structure, where each titanium atom is sandwiched between selenium layers, forming a quasi-two-dimensional system (Fig. 1a, b). At ambient pressure, $TiSe_2$ undergoes a CDW transition at $T_{CDW} \approx 200$ K[4,5] (Fig. 1d), and upon electron doping (e.g., through Cu intercalation) or pressure application, the CDW is suppressed and superconductivity emerges[5–8]. The pressure-induced phase diagram of *1T*-$TiSe_2$, illustrating the interplay between CDW suppression and superconductivity, is shown in Fig. 1c.

Although previous studies have explored the role of excitonic interactions and electron-phonon coupling in $TiSe_2$, recent quantum oscillation measurements and electronic structure calculations suggests that a Lifshitz transition, a topological change in the Fermi surface, plays a key role in stabilizing the superconducting phase[5]. The relationship between superconductivity and the suppression of CDW order remains an open question. Theoretical models suggest that the reconstruction of the electronic structure near the critical point of the CDW could give rise to new pairing mechanisms, potentially leading to an unconventional multi-gap state[9,10]. In particular, Hinlopen et al.[5] recently identified a Lifshitz transition in $TiSe_2$ coinciding with the emergence of superconductivity, reinforcing the idea that Fermi surface topology strongly influences pairing interactions. However, the microscopic nature of the superconducting state and its direct connection to these changes in the electronic structure remain to be fully elucidated.

Here, we investigate the superconducting gap structure of *1T*-$TiSe_2$ under hydrostatic pressure using transverse field (TF) muon spin rotation/relaxation (μ^+SR). The finely tunable muon momentum enables precise stopping at specific depths, allowing the muons to penetrate the thick walls of the pressure cell and directly target the sample. This makes μ^+SR particularly well suited for determining the superconducting properties of *1T*-$TiSe_2$ under pressure. Our results provide direct evidence for a two-gap superconducting state, where the smaller gap exhibits a disproportionately high superfluid density contribution. This observation is consistent with the emergence of additional Fermi surface pockets at the Lifshitz transition, a phenomenon seen in other multigap superconductors such as MgB_2, $NbSe_2$, and $FeSe_{1-x}$[11–14]. These findings establish a direct link between pressure-induced Fermi surface evolution and the superconducting state in *1T*-$TiSe_2$, shedding new light on the interplay between CDW order, band structure reconstruction, and multigap superconductivity in layered quantum materials.

Results

Disentangling the μ^+SR signal: sample vs. pressure cell

μ^+SR is an essential technique in the measurement of a superconductors superfluid density. However, when measuring under pressure, a key challenge is to isolate the sample response from the temperature-dependent background of the pressure cell, as the superconducting signal is low compared to the pressure cell. To achieve this, measurements were taken below and above

[1]Department of Applied Physics, KTH Royal Institute of Technology, SE-106 91 Stockholm, Sweden. [2]PSI Center for Neutron and Muon Sciences CNM, 5232 Villigen PSI, Switzerland. [3]Physik-Institut, Universität Zürich, Winterthurerstrasse 190, CH-8057 Zürich, Switzerland. [4]Department of Physics, Chalmers University of Technology, Göteborg, SE-412 96, Sweden. [5]Department of Physics and Astronomy, Uppsala University, Box 516, SE-75120 Uppsala, Sweden. [6]Department of Applied Physics and Astronomy, University of Sharjah, P. O. Box 27272, Sharjah, United Arab Emirates. ✉e-mail: elson@kth.se; sassa@kth.se; condmat@kth.se

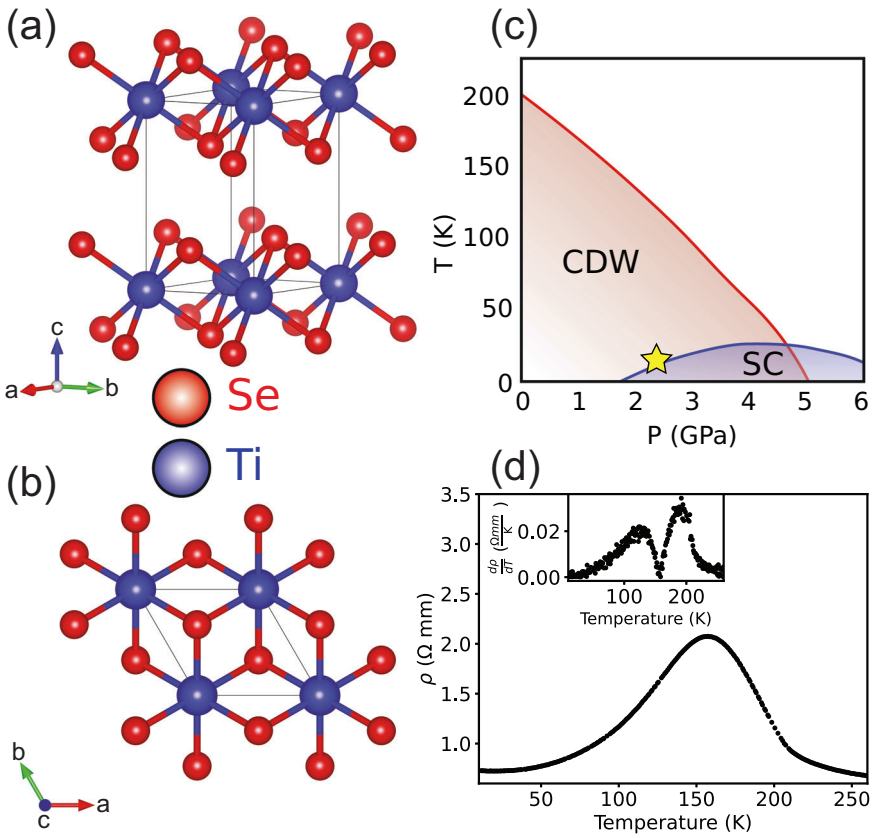

Fig. 1 | Crystal structure and schematic phase diagram of *1T*-$TiSe_2$ as a function of pressure. **a** The layered hexagonal structure of *1T*-$TiSe_2$, with each unit cell containing a single layer. Titanium (blue) and selenium (red) atoms are represented by spheres proportional to their atomic radii. **b** View of the *a*-*b* plane, showing the trigonal arrangement of layers characteristic of the *1T* polymorph. **c** The phase diagram of *1T*-$TiSe_2$ under hydrostatic pressure, showing the overlap of the CDW and the superconducting (SC) phases (an interpretation of the data in ref. 5). The yellow star indicates the pressure used for the μ^+SR experiment. **d** The temperature dependence of resistivity measured at zero magnetic field. The lower inset highlights the derivative of the resistivity, marking the CDW transition.

the superconducting transition (0.27 K < T_C ≈ 1.8 K < 2.3 K) at two muon implantation momentum of 95 MeV/c and 100 MeV/c. The use of two distinct momenta enhances our ability to discern the pressure cell background, as lower-momentum muons (95 MeV/c) primarily stop within the pressure cell, while higher-momentum muons (100 MeV/c) stop in both the pressure cell and the sample. Fitting the data from both momenta at each temperature point under the given pressure allows for a more accurate separation of the pressure cell contribution. This approach is further supported by simulations conducted with a custom tool described in ref. 15, which employs the Transport of Ions in Matter TRIM package[16]. The description of the pressure cell and input parameters for the simulations are detailed in the Methods section. The results of the simulations for our *1T*-$TiSe_2$ pressure experiment indicate that at 95 MeV/c, only 6.55% of the muons stop within the sample, whereas at 100 MeV/c, 35.26% of the muons reach the sample. Such evaluation helps defining a proper fitting procedure, as the 95 MeV/c data will have contributions primarily from the pressure cell, whilst the 100 MeV/c data will have significant contributions from both the sample and pressure cell.

Temperature-dependent depolarization rates

To observe the formation of the vortex lattice, the *1T*-$TiSe_2$ sample was field-cooled from above the superconducting transition temperature down to T = 0.27 K in the presence of an external magnetic field of B = 100G. This field-cooling process ensures the establishment of the vortex lattice in the superconducting state. The spin polarization $P(t)$ of the muons was subsequently measured as a function of time at two distinct temperatures (T = 2.3 K and T = 0.27 K), under ambient pressure (P_{amb} = 0 kbar) and maximum applied pressure (P_{max} = 23.0 kbar). The transverse-field μ^+SR time spectra recorded for these conditions are shown in Fig. 2. The data reveals differences in the oscillatory behavior of $P(t)$ between the two pressures. At P = 23.0 kbar and T = 0.27 K (Fig. 2a), the oscillations exhibit pronounced damping compared to the spectra at P = 0 kbar and T = 0.27 K, which is a direct signature of the formation of a vortex lattice under high pressure. As a comparison, at T = 2.3 K, well above (T_c), the oscillations do not display any damping difference between the two pressures, reflecting the absence of the vortex state (Fig. 2b). When cooling significantly below T_c down to base temperature (T = 0.27 K), a notable increase in the damping is observed, consistent with the continuous rise of the total depolarization rate σ_T (Fig. 2c). The spectra were analyzed using the following fitting model:

$$\begin{aligned} A_0 P(t) \;=\; & (A_T - A_S)\cos\left(2\pi B_{PC}\gamma_\mu t + \tfrac{\pi\phi}{180}\right) \\ & \cdot e^{-\frac{1}{2}(\sigma_{PC}t)^2} e^{(-\lambda_{PC}t)} \\ & + A_S \cos\left(2\pi B_S \gamma_\mu t + \tfrac{\pi\phi}{180}\right) e^{-\frac{1}{2}(\sigma_S t)^2}, \end{aligned} \tag{1}$$

where A_T is the total asymmetry, A_S is the sample asymmetry, B_{PC} is the field inside the pressure cell, γ_μ is the muon gyromagnetic ratio, ϕ is the phase offset, σ_{PC} is the depolarization rate from the pressure cell, λ_{PC} is the relaxation rate from the pressure cell, and σ_S is the depolarization rate from the sample. This model accounts for contributions from both the sample and the pressure cell. The first term represents the pressure cell contribution, characterized by the depolarization rate σ_{PC} and relaxation rate λ_{PC}, while the second term captures the sample contribution, with the depolarization rate σ_S. For the 95 MeV/c dataset, A_S was set to zero, as very few muons are expected to stop within the sample at this momentum. We used an iterative fitting process, with the saturating parameters held fixed. In this process, for the 100 MeV/c dataset, A_S was fixed at 0.1 to reduce the number of free parameters and improve the robustness of the fit. Across all four dataset (P = 23.0 kbar, P = 0 kbar, 95 MeV/c, and 100 MeV/c), A_T, and σ_{PC} were fitted as global parameters across all temperatures. For a given temperature at both momenta and pressures, ϕ (phase offset), B_{PC} (field inside the pressure cell), and λ_{PC} (pressure cell relaxation rate) were kept constant, while the remaining parameters were fitted independently for each momentum and pressure condition. This fitting strategy allows to isolate the pressure cell response, which is shown in Fig. 3a. The temperature dependence of λ_{PC}

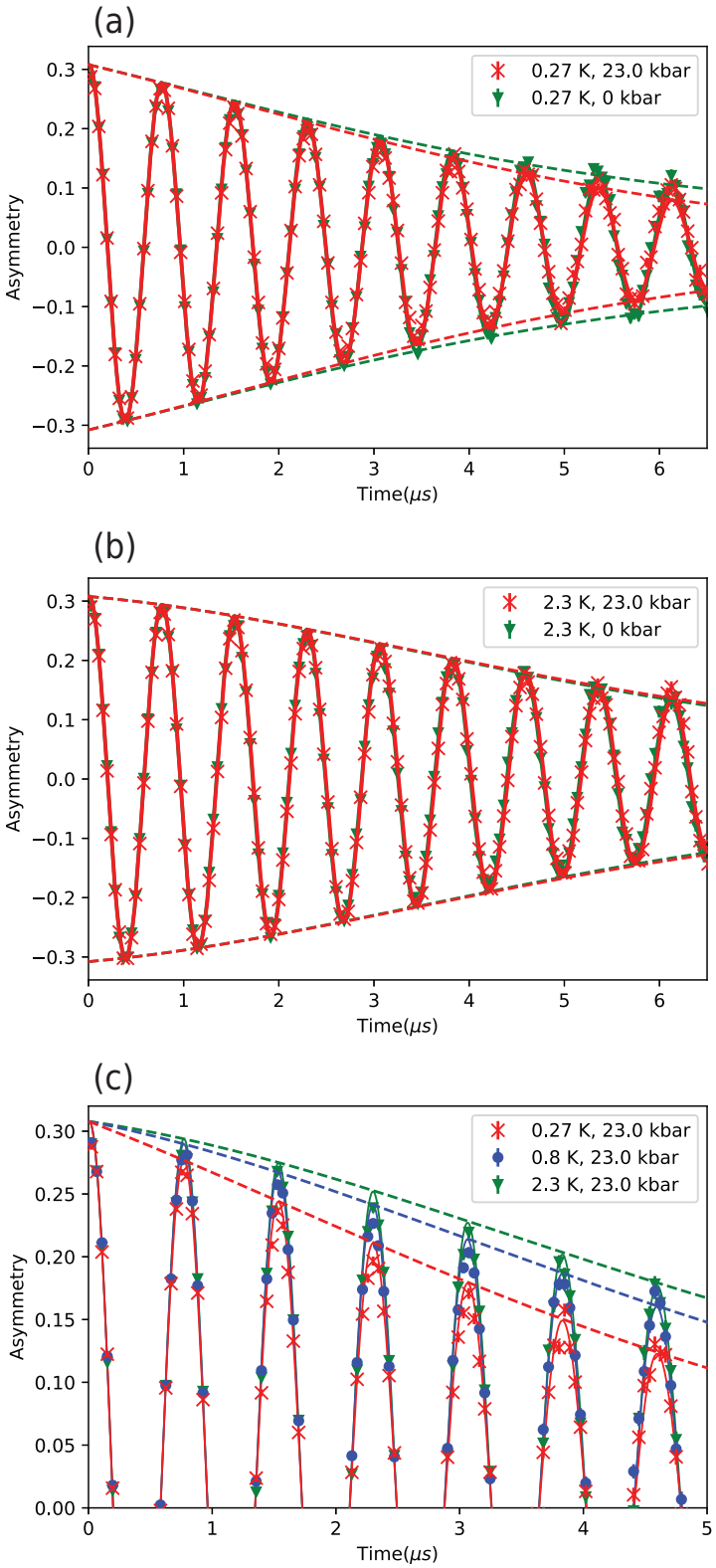

Fig. 2 | Transverse-field μ^+SR time spectra of $TiSe_2$ in a 100 Gauss applied field. Data points represent measurements at $P = 23.0$ kbar and $P = 0$ kbar, taken at two temperatures: **a** $T = 0.27$ K (within the superconducting state) and **b** $T = 2.3$ K (above the superconducting transition). Panel **c** shows the muon spectra for three temperatures ($T = 0.25$, 0.8, 2.3 K) at $P = 23.0$ kbar. The solid lines correspond to fits to the experimental data, highlighting differences in the magnetic field distribution due to the formation of a vortex lattice at high pressure and low temperature.

exhibits a similar behavior to that reported in ref. 17, confirming the consistency of the pressure cell signal.

The temperature dependence of the depolarization rate from the sample at both high and zero pressure is extracted and shown in Fig. 3b. At zero pressure, the depolarization rate remains nearly constant down to the lowest temperature. This behavior is consistent with a non-superconducting state, where the depolarization rate is dominated by a constant contribution from randomly ordered nuclear moments. The zero-pressure depolarization rate has been fitted to a constant value of $\sigma_n = 0.112 \pm 0.002\ \mu s^{-1}$, which represents the nuclear contribution. In contrast, the data at $P = 23.0$kbar exhibit a significant increase in the depolarization rate below $T_c = 1.8$ K. This transition is similar to $x = 0.05$ in Cu_xTiSe_2[6], indicating the onset of the

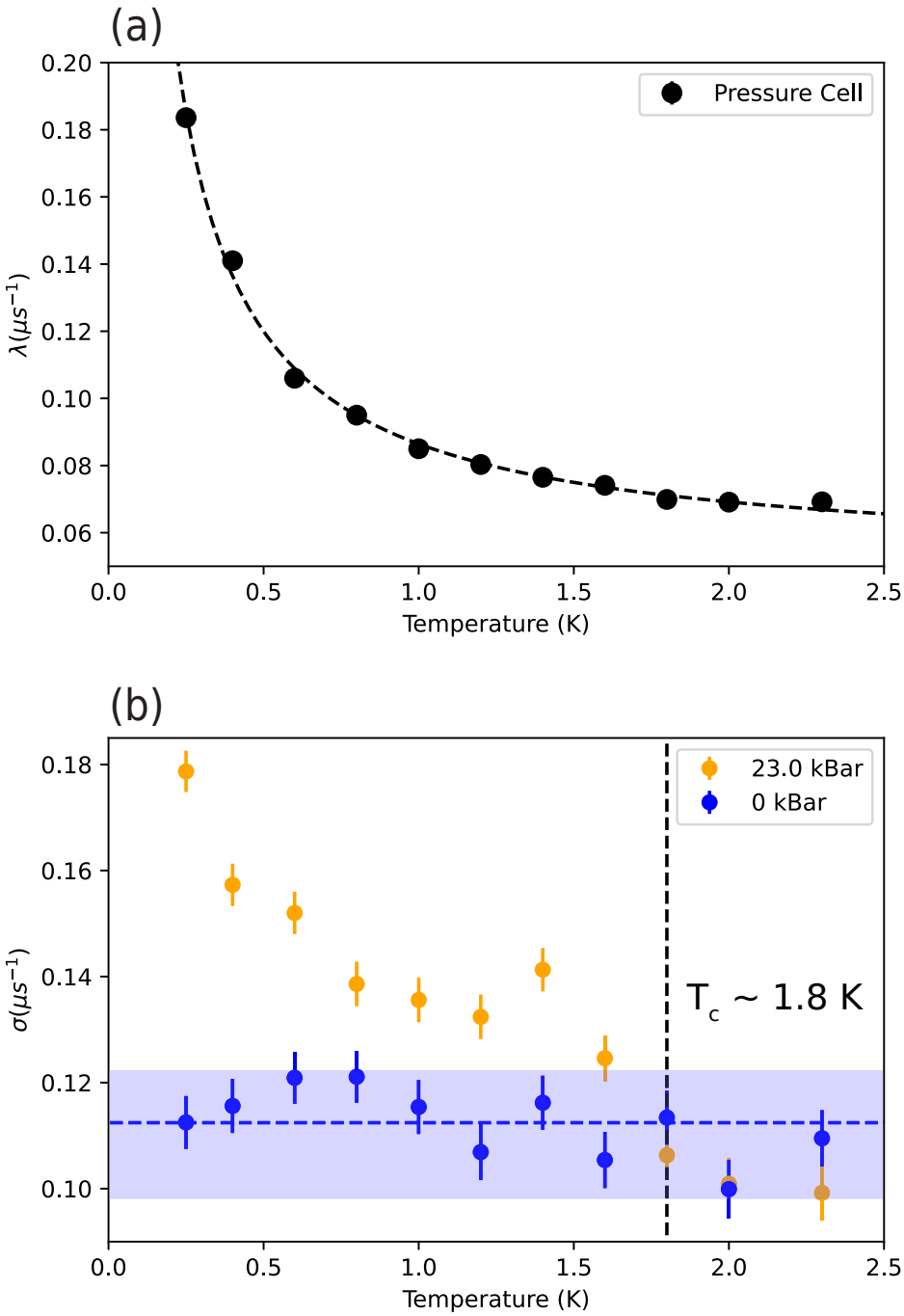

Fig. 3 | Temperature dependence of key fit parameters. a The temperature dependence of the relaxation rate of the MP35N pressure cell, fitted as a global parameter for all data sets. This shows excellent agreement with previously reported values from the literature[17]. **b** Temperature dependence of the muon depolarization rate originating from the sample, measured at both high pressure (orange) and zero pressure (blue). The data highlight the increase in depolarization rate below $T_c \approx 1.8$ K under high pressure, indicative of the formation of a superconducting vortex lattice.

superconducting transition and formation of the vortex lattice in the high-pressure state.

Evidence for dual-gap superconductivity

The muon spin depolarization rate in the superconducting state contains contributions from both the vortex lattice (σ_{SC}) and the nuclear magnetic moments (σ_n). The total depolarization rate is expressed as[18]:

$$\sigma_T^2 = \sigma_{SC}^2 + \sigma_n^2. \quad (2)$$

The contribution from the superconducting vortex lattice (σ_{SC}) is extracted by subtracting the nuclear contribution (σ_n) from the total depolarization rate (σ_T). The previously determined value, $\sigma_n = 0.112 \pm 0.002\ \mu s^{-1}$, was used for this subtraction to maintain physical consistency. To avoid negative values under the square root, any high-pressure data points yielding results below $0.112\ \mu s^{-1}$ were set to zero.

Building on the temperature dependence of σ_{SC}, we next relate to the penetration depth, λ_L, providing insights into the superconducting gap structure. In our TF-μ^+SR geometry the depolarization signal is primarily sensitive to the in-plane penetration depth λ_{ab}, which dominates in quasi-two-dimensional $TiSe_2$. No explicit corrections for vortex lattice disorder or demagnetization were applied, as the measurements were performed in a low applied field (100 G) under field-cooled conditions, minimizing disorder effects. After subtracting the temperature-independent nuclear contribution, the superconducting depolarization rate $\sigma_{SC}(T)$ was used directly to determine the normalized superfluid

density. The superfluid density is defined by the following relation[19]:

$$\frac{\lambda_L^2(0)}{\lambda_L^2(T)} \propto \frac{\sigma_{SC}(T)}{\sigma_{SC}(0)} = 1 + \frac{1}{\pi}\int_0^{2\pi}\int_{\Delta_k}^{\infty} \frac{E}{\sqrt{E^2-{\Delta_k}^2}}\frac{\partial f}{\partial E}\, dE d\phi, \tag{3}$$

where $f = \left[1+\exp\frac{E}{k_BT}\right]^{-1}$ is the Fermi- Dirac distribution, and $\Delta_k = \Delta(T)$ $g(\phi)$ describes the temperature and angular dependence of the superconducting gap. For an *s*-wave symmetry, we assume $g(\phi) = 1$, as an *s*-wave gap should be uniform in momentum space[20].

Further, defining the quasiparticle energy as $E = \sqrt{\varepsilon^2+\Delta^2}$, where ε is the normal metal band energy from the Fermi level, we obtain the equation used in our fitting procedure for an *s*-wave superconducting gap[21]:

$$\frac{\sigma_{SC}(T)}{\sigma_{SC}(0)} = 1 - \frac{1}{2k_BT}\int_0^{\infty} \cosh^{-2}\left(\frac{\sqrt{\varepsilon^2+\Delta(T)^2}}{2k_BT}\right) d\varepsilon, \tag{4}$$

For the temperature-dependent superconducting gap, we use the BCS expression[22]:

$$\Delta(T) = \Delta(0)\tanh\left[1.821\times\left(1.018\left(\frac{T_c}{T}-1\right)\right)^{0.51}\right],$$

where $\Delta(0)$ is the maximum gap value at $T = 0$. From BCS theory[20], the predicted maximum gap size for a conventional BCS superconductor is $\Delta(0) = 1.764 k_B T_c$, which in our case gives $\Delta(0) \approx 0.25$ meV. However, when fitting our data to a single-gap model, we obtain a gap size of $\Delta(0) = 0.34 \pm 0.09$ meV, which is significantly larger than the BCS prediction. This discrepancy suggests that a simple BCS model may not fully describe the superconducting behavior.

Observations from other two-gap superconductors, such as those discussed in ref. 19, show a similar nearly linear increase in the depolarization rate at low temperatures, suggesting the presence of two distinct superconducting gaps.

To account for this behavior, we fit the data using a two-gap *s*-wave model. The total superconducting depolarization rate is expressed as:

$$\frac{\sigma_{SC}(T)}{\sigma_{SC}(0)} = \omega\frac{\sigma_1(T)}{\sigma_1(0)} + (1-\omega)\frac{\sigma_2(T)}{\sigma_2(0)}, \tag{5}$$

where ω represents the weight of the contribution from each superconducting gap. A fit to Eq. (5) for the temperature dependence of σ_{SC} is shown in Fig. 4. Here, $T_c = 1.8$ K was fixed, and the following fit parameters were obtained: $\omega = 0.546 \pm 0.082$, $\Delta(0)_1 = 0.057 \pm 0.027$ meV, $\Delta(0)_2 = 0.705 \pm 0.208$ meV, and $\sigma_0 = 0.161 \pm 0.037\ \mu s^{-1}$. The maximum errors for the fit are indicated in Fig. 4 (dashed purple lines). For completeness, we also tested single-gap *s*-, anisotropic *s*-, and *d*-wave models, as well as two-gap $d+s$ and $d+d$ scenarios. These alternative fits either fail to reproduce the low-temperature behavior of $\sigma_{SC}(T)$ or require unphysical parameters, as shown in the Supplementary Information (Fig. S1). To test whether the two-gap fit simply benefits from additional parameters, we quantitatively compared all models (single-*s*, *d*, anisotropic-*s*, $d+d$, $s+d$, and $s+s$) using the same dataset (Supplementary Fig. S1 and Table S1). The reduced χ^2 values are: single-$s = 7.156$, $d = 4.581$, anisotropic-$s = 3.574$, $d+d = 1.483$, $s+d = 1.484$, and $s+s = 1.392$ (best). Thus, the $s+s$ model lowers χ_ν^2 by factors of ~ 2.6–5 relative to single-gap fits. Applying $\Delta\mathrm{AIC} = 2\Delta k + n\ln(\chi^2_{\nu,\mathrm{model}}/\chi^2_{\nu,s+s})$ shows that even for modest data sets ($n \gtrsim 5$) the improvement remains statistically significant after penalizing the extra parameter count.

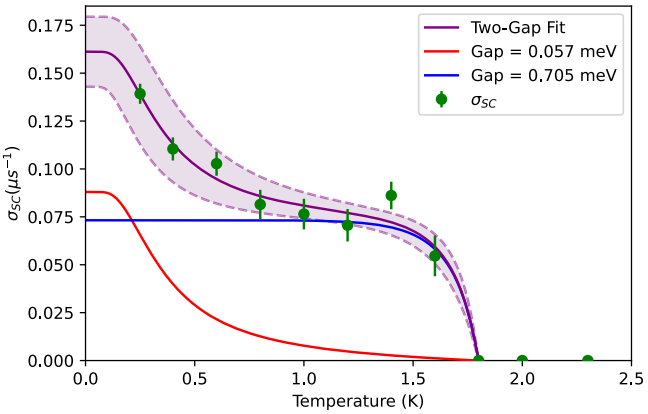

Fig. 4 | Temperature dependence of the superconducting depolarization rate in $TiSe_2$ arising from the formation of the vortex lattice. The solid purple line represents a fit to a two-gap model, accurately capturing the kink in the results. The dashed purple lines illustrate the maximum uncertainties of the fit. The red and blue lines correspond to the contributions from the individual superconducting gaps, highlighting their distinct roles in shaping the overall depolarization behavior.

Anisotropic-*s* fits require extreme anisotropy ($\Delta_{min}/\Delta_{max} \lesssim 0.2$) to mimic the observed curvature and still fail to reproduce the low-temperature kink near 1.3 K, whereas the fully gapped two-band $s+s$ model reproduces the data with physically reasonable parameters. We therefore identify the two-gap $s+s$ model as the most consistent description of $\sigma_{SC}(T)$.

While the two-gap $s+s$ model fit effectively captures the observed behavior, it is worth noting the scattered value at $T = 1.5$K, which can be attributed to variations in the nuclear depolarization rate σ_n, expected to fluctuate within a range of 0.01. Also, at temperatures below $T = 0.5$K, the relaxation rate from the pressure cell (as described in ref. 17) increases significantly, overlapping with the temperature range where the superconducting depolarization rate rises. However, since the relaxation rate of the pressure cell was well-accounted for through the two-momentum fitting procedure, we can confidently attribute the observed two-gap behavior primarily to the sample.

Discussion

The dual-gap behavior observed in pressurized 1*T*-$TiSe_2$ provides compelling evidence for multi-band superconductivity. The temperature dependence of the muon spin depolarization rate, which reflects the magnetic penetration depth and thereby the superfluid density, can only be consistently described within a two-gap model. This behavior is reminiscent of other multiband superconductors, such as MgB_2, $NbSe_2$, and $FeSe_{1-x}$[11–14]. In MgB_2, the larger gap, $2\Delta_\sigma/k_BT_c \approx 4.3$, resides on the quasi-two-dimensional σ-bands derived from in-plane B-B bonding, while a smaller gap, $2\Delta_\pi/k_BT_c \approx 1.6$, opens on the three-dimensional π-bands[11,23]. Similarly, in $FeSe_{1-x}$ under pressure, the smaller gap yields $2\Delta/k_BT_c$ values in the range 0.9-1.4[14]. For pressurized $TiSe_2$, our extracted gap values, $2\Delta_1/k_BT_c \approx 0.73$ and $2\Delta_2/k_BT_c \approx 9.1$, deviate strongly from the single-band weak-coupling BCS value of 3.52, indicating the coexistence of a weakly coupled regime with pronounced interband asymmetries. The disparity between the two gaps in $TiSe_2$ is more extreme than in MgB_2 or $FeSe_{1-x}$, yet it still falls within the broad range reported for other multigap superconductors. Comparable values of $2\Delta/k_BT_c \sim 7$–10 have been observed in $Ba_{0.6}K_{0.4}Fe_2As_2$ (~ 7–9)[24,25], reflecting band-selective strong coupling in multigap systems. Furthermore, ref. 26 finds that the Lifshitz transition generates a strongly orbital-renormalized pocket, whose altered effective mass could naturally explain the superfluid-density imbalance.

Furthermore, μ^+SR measurements on MgB_2 reveal that the superfluid density at low temperatures is dominated by the σ-bands, owing to their stronger electron-phonon coupling and higher in-plane Fermi velocity, while the π-bands contribute significantly only in the vicinity of T_c[23]. In contrast, our data on pressurized $TiSe_2$ demonstrate the opposite trend: the

smaller gap contributes disproportionately to the total superfluid density λ_L^{-2}. This observation suggests that the associated band possesses either a large density of states (DOS) or a higher carrier concentration.

Such a scenario is qualitatively consistent with a pressure-induced Lifshitz transition, whereby new Fermi-surface pockets emerge as bands cross the Fermi level[5,27]. These transitions are known to sharply enhance the DOS near E_F and, as shown theoretically, can increase the superfluid density in the newly formed band[28]. This mechanism can be understood quantitatively by considering that the superfluid density, ρ_{SC}, in a multiband superconductor is proportional to the weighted integral over the quasiparticle density of states $N(E)$ and the Fermi distribution function $f(E)$:

$$\rho_{SC} \propto \int N(E) f(E)\, dE. \tag{6}$$

When a new band crosses the Fermi level, the enhanced $N(E)$ can cause even a smaller-gap condensate to dominate the stiffness. Similar Lifshitz-transition-driven effects have been reported in other multiband superconductors near CDW or spin-density-wave instabilities[29,30]. Furthermore, Lifshitz-driven enhancements of the density of states can be understood in the broader context of Fermi-surface instabilities, analogous to the crucial role played by van Hove singularities in shaping the electronic structure and phase behavior of $Sr_4Ru_3O_{10}$[31].

Recent DFT calculations show that $TiSe_2$ undergoes a significant electronic reconstruction around 20 kbar[5], consistent with the pressure range of our measurements. In particular, new electron pockets at the L point and hole pockets at Γ emerge just as superconductivity sets in[5]. A detailed account of the Fermi-surface evolution in $TiSe_2$ under pressure, including the emergence of these new pockets, has been reported by Hinlopen et al.[5], and we refer the reader to their work for further clarity. The smaller-gap band is likely linked to one of these pockets, whose enhanced DOS explains its prominent role in the superfluid response.

While the Lifshitz-driven enhancement of the DOS provides a natural explanation, in multiband superconductors the stiffness is also shaped by factors beyond DOS and gap magnitude. Within the two-band BCS/Eliashberg framework[10,32], the weighting of each band's contribution depends on its carrier density-to-effective-mass ratio (n/m^*), momentum-dependent coherence factors, and the strength of interband scattering. Strong interband coupling tends to homogenize gap magnitudes and distribute stiffness more evenly across bands, whereas weak coupling allows one band, even with a smaller gap, to dominate[29]. Effective mass renormalization, as may occur in nearly flat bands near a Lifshitz transition, can further amplify this effect[28]. In pressurized $TiSe_2$, reduced interband hybridization and possible mass enhancement near the CDW critical point would reinforce the dominance of the smaller-gap condensate. Also, in weakly coupled two-gap systems, relative phase fluctuations between condensates can give rise to low-energy Leggett modes[33], which, while not directly accessible to μ^+SR, could still influence the stiffness. The smooth temperature dependence of $\sigma_{SC}(T)$ in our data is, however, more consistent with phase-locked condensates. Lastly, the proximity to a suppressed CDW phase suggests that residual fluctuations may promote a sign-changing $s_\pm$ order parameter[29,34]. Although μ^+SR cannot detect the relative gap phase, the observed two-gap structure and its pressure evolution remain compatible with such an unconventional pairing state.

Our findings also provides a broader relationship between superconductivity and the suppression of CDW order in $TiSe_2$. While long-range CDW order vanishes under pressure, residual fluctuations or domain structures may persist[35]. These incommensurate modulations can serve as a backdrop for unconventional pairing, particularly in systems with electron and hole pockets connected by the former CDW wavevector[36]. This environment is naturally conducive to $s_\pm$ gap symmetry, wherein the superconducting order parameter changes sign between disconnected Fermi surfaces. It is thus instructive to compare this clean tuning by pressure with chemical doping. In Cu_xTiSe_2, ARPES reveals a chemical-potential shift, progressive suppression of the CDW gap, and growth of the L-point electron pocket with increasing x[37–39]. By contrast, under pressure the Fermi-surface changes are driven mainly by lattice and orbital hybridization, with little chemical-potential drift[5,27]. Equally important, Cu intercalation introduces disorder through interlayer Cu sites, which broadens ARPES/STM spectral features and enhances interband scattering[10,29]. Indeed, STM/STS on Cu_xTiSe_2 reveals nanoscale gap inhomogeneity[8], and μ^+SR measurements required anisotropic s-wave fits without resolving separate gaps[8]. To our knowledge, the anomalous weighting of the superfluid density by the smaller-gap band has not been reported in Cu_xTiSe_2, suggesting that it is either absent or masked by disorder. Pressure, being a cleaner tuning parameter, thus reveals the unusual dominance of the smaller gap more sharply.

Finally, the pressure-induced Fermi surface reconstruction in $TiSe_2$ may also carry topological implications. In transition metal dichalcogenides, strong spin-orbit coupling and band inversions near high-symmetry points can produce Berry curvature hotspots and, in some cases, topologically nontrivial electronic states[40,41]. DFT calculations under pressure indicate that new electron and hole pockets appear at the L and Γ points in $TiSe_2$[5]; if these states derive from inverted bands or are strongly spin-orbit coupled, they could host finite Berry curvature. Although μ^+SR is insensitive to Berry curvature directly, such topological features could influence superconductivity through modified interband scattering or even by supporting topological superconducting phases[42]. While speculative, this possibility situates pressurized $TiSe_2$ within the broader class of materials where Fermi surface topology and superconductivity are intimately linked. Furthermore, recent theoretical studies show that fluctuating pair-density-wave order can give rise to superconductivity in which both the gap amplitude and transition temperature decay monotonically with increasing superfluid stiffness[43], a trend reminiscent of our observation in here. Although distinct from our present findings, such ideas raise the possibility that pressure-tuned $TiSe_2$ may share common threads with a broader family of unconventional and vestigial superconducting phases.

In summary, our μ^+SR measurements demonstrate that two-gap superconductivity in pressurized $1T$-$TiSe_2$ is closely tied to the suppression of CDW order and the associated Fermi-surface reconstruction. The unusually strong contribution from the smaller gap likely reflects a Lifshitz-transition-enhanced density of states. These results position $TiSe_2$ as a model system for exploring how subtle changes in electronic topology and residual charge order can stabilize unconventional superconductivity in layered materials. Future μ^+SR experiments spanning a broader range of pressures will be essential to track how the two-gap structure evolves across the superconducting dome and relative to the CDW critical point.

Methods

Sample growth and preparation

High-quality millimeter-sized crystals of $1T$-$TiSe_2$ were grown via solvent evaporation from a metal-saturated chalcogen solvent at temperatures exceeding 827 °C. A detailed description of the growth process for $1T$-$TiSe_2$ single crystals can be found in ref. 4.

For the μ^+SR experiment under pressure, the single crystals were crushed into a fine powder, which was then pressed into a cylindrical pellet measuring 13 mm in length and 6 mm in diameter. The pellet was loaded into a pressure cell, with Daphne oil serving as the pressure-transmitting medium[44]. The pressure cell employed in the experiment was a double-wall design fabricated from MP35N alloy. At the bottom of the cell, a piece of indium was included to estimate the applied pressure. The schematic of the pressure cell is shown in Fig. 5a.

The pressure was determined by measuring the AC magnetic susceptibility of the indium as a function of temperature. The applied pressure was then calculated from the superconducting transition temperature of indium using the following relationship[45]

$$T_c(P) = -0.0346P + T_c(0) \tag{7}$$

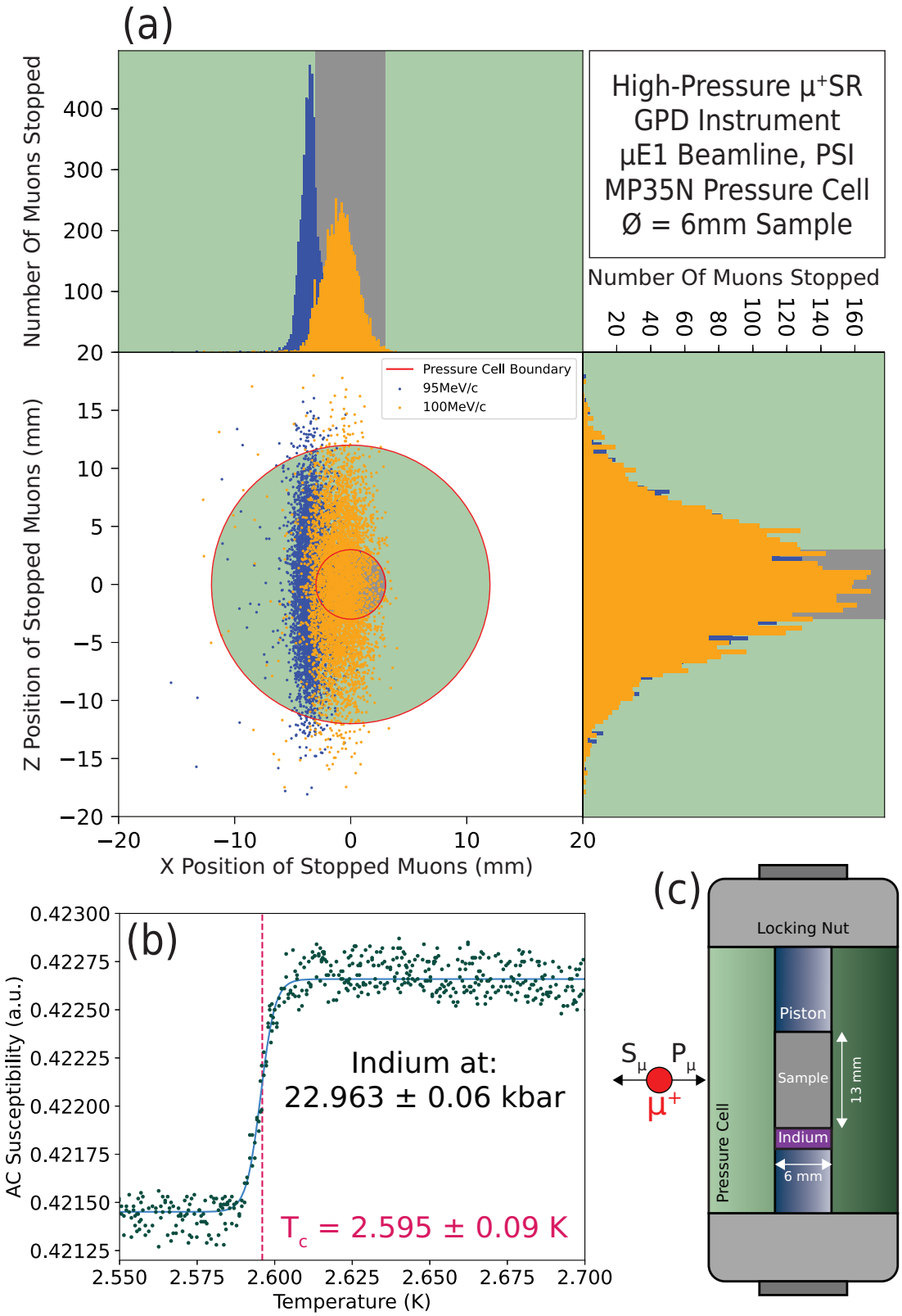

Fig. 5 | Pressure cell, muon stopping simulations, and ac susceptibility curve of indium located at the bottom of the pressure cell. a Schematic representation of the MP35N pressure cell in the X-Z plane, illustrating the experimental setup. Simulations[15] indicate that 6.55% of the muons stop in the sample at 95 MeV/c, while 35.26% stop in the sample at 100 MeV/c, demonstrating the dependence of muon implantation efficiency on beam momentum. **b** The superconducting transition temperature, measured as $T_c = 2.595 \pm 0.009$ K, is indicated by the sharp drop in magnetic susceptibility. This corresponds to an applied pressure of $P = 22.963 \pm 0.06$ kbar at the base temperature. **c** A detailed graphical depiction of the MP35N pressure cell employed at the GPD instrument, highlighting the sample position and other critical components such as the piston, locking nut, and indium to determine the applied pressure.

where P is hydrostatic pressure in kbar and $T_c(0)$ = 3.39 K, the superconducting transition temperature of indium at ambient pressure. The pressure was therefore fitted to be P =22.963 ± 0.06 kbar, as shown in Fig. 5c. The pressure is quoted as $P \approx 23.0$ kbar to reflect the precision consistent with the hydrostatic conditions across the sample. The MP35N pressure cell employed in this study operates close to its authorized mechanical limit. To achieve $P_{base} \simeq 23$ kbar at low temperature, a room-temperature setpoint of $P_{RT} \approx 25$ kbar must be applied, which represents the highest pressure compatible with safe operation and facility authorization. Higher setpoints risk irreversible damage to the cell and are therefore not permitted. Importantly, $P \simeq 23$ kbar lies precisely in the vicinity of the Lifshitz transition identified by DFT and quantum-oscillation studies[5], i.e. the regime where the anomalous stiffness weighting is expected to be maximal. We have thus focused on this single, most relevant pressure point while explicitly acknowledging in the Discussion that future μ^+SR experiments across multiple pressures will be essential when beamtime and hardware allow.

The simulation[15] replicates the experimental environment, including the dimensions and compositions of the pressure cell and sample. The muon beam parameters, such as momenta (here, 95 MeV/c and 100 MeV/c), are input to simulate the trajectories, energy loss, and stopping locations of the muons. The tool then utilizes TRIM simulations to calculate the fractions of muons that stop in each region (e.g., pressure cell vs. sample), enabling a precise determination of background contributions (Fig. 5b). To account for the MP35N pressure-cell contribution, we analysed the 95 MeV/c and 100 MeV/c datasets simultaneously. In this global fitting procedure, the pressure-cell relaxation parameters (σ_{PC}, λ_{PC}) were constrained across all temperatures, while only the sample-related depolarization rate (σ_S) was allowed to vary. This strategy reliably separates the background signal from the superconducting response and prevents spurious temperature-dependent effects from the pressure cell from being misattributed to the sample.

Muon spin resonance (μ^+SR) experiment

The μ^+SR measurements were taken at the General Purpose Decay-Channel Spectrometer (GPD) instrument on the μE1 beamline at the Paul Scherrer Institute (PSI) in Villigen, Switzerland. All measurements were taken in a field cooled environment in a 100 Gauss field, as this allows us to see clear damped oscillations whilst being above H_{c1} and below H_{c2}, perpendicular to the muons momentum. To analyse the data, the software package musrfit[46] was used. A temperature down to 0.25 K was achieved using a helium-3 insert in the VARIOX cryostat.

Vortex state protocol in μ^+SR

In type-II superconductors, such as Cu-doped or pressurized *1T*-$TiSe_2$, an applied magnetic field partially penetrates the material, forming quantized magnetic flux lines arranged in a lattice structure called the vortex state. The μ^+SR technique is particularly well-suited for studying the microscopic magnetic field distribution in the vortex state, as it is highly sensitive to inhomogeneous magnetic fields. In a transverse-field μ^+SR experiment, an external magnetic field is applied perpendicular to the initial muon spin polarization. This experimental setup allows for the measurement of the depolarization rate (σ) as a function of temperature. The depolarization rate is directly proportional to the second moment of the local magnetic field distribution and inversely proportional to the square of the London penetration depth (λ_L), which reflects the superfluid density in the superconducting state. Mathematically, σ is related to the penetration depth as $\sigma \propto \frac{1}{\lambda_L^2}$, where λ_L characterizes how magnetic fields decay within the superconductor. This relationship provides crucial insights into the superconducting gap structure and underlying pairing mechanisms.

Data availability

Data and their analysis are available from the corresponding authors upon reasonable request. The raw data is also available through the "http://musruser.psi.ch/" webpage.

Received: 14 May 2025; Accepted: 23 November 2025;
Published online: 15 December 2025

References

1. Manzeli, S. et al. 2d transition metal dichalcogenides. *Nat. Rev. Mater.* **2**, 17033 (2017).
2. Monney, C. et al. Probing excitonic insulator phase in tise2. *Phys. Rev. B* **81**, 115114 (2010).
3. Kusmartseva, A. F., Sipos, B., Berger, H., Forró, L. & Tutiš, E. Pressure Induced Superconductivity in Pristine 1*T*-$TiSe_2$. *Phys. Rev. Lett.* **103**, 236401 (2009).
4. Chareev, D. A. et al. Growth of Transition-Metal Dichalcogenides by Solvent Evaporation Technique. *Crystal Growth & Design* **20**, 6930–6938 (2020).
5. Hinlopen, R. D. H. et al. Lifshitz transition enabling superconducting dome around a charge-order critical point. *Science Advances* **10**, eadl3921 (2024).
6. Morosan, E. et al. Superconductivity in Cu_xTiSe_2. *Nature Phys.* **2**, 544–550 (2006).
7. Hillier, A. D. et al. Probing the superconducting ground state near the charge density wave phase transition in $Cu_{0.06}TiSe_2$. *Phys. Rev. B* **81**, 092507 (2010).
8. Zaberchik, M. et al. Possible evidence of a two-gap structure for the Cu_xTiSe_2 superconductor. *Phys. Rev. B* **81**, 220505 (2010).
9. Fradkin, E., Kivelson, S. A. & Tranquada, J. M. Colloquium: Theory of intertwined orders in high temperature superconductors. *Rev. Mod. Phys.* **87**, 457–482 (2015).
10. Gurevich, A. Enhancement of the upper critical field by nonmagnetic impurities in dirty two-gap superconductors. *Phys. Rev. B* **67**, 184515 (2003).
11. Souma, S. et al. The origin of multiple superconducting gaps in MgB_2. *Nature* **423**, 65–67 (2003).
12. Sassa, Y. et al. Probing two- and three-dimensional electrons in mgb_2 with soft x-ray angle-resolved photoemission. *Phys. Rev. B* **91**, 045114 (2015).
13. Dvir, T. et al. Spectroscopy of bulk and few-layer superconducting nbse2 with van der waals tunnel junctions. *Nature Communications* **9**, 598 (2018).
14. Khasanov, R. et al. Evolution of Two-Gap Behavior of the Superconductor $FeSe_{1-x}$. *Phys. Rev. Lett.* **104**, 087004 (2010).
15. Elson, F. et al. TRIM Simulations Tool for $\mu+$ Stopping Fraction in Hydrostatic Pressure Cells. *Journal of Physics: Conference Series* **2462**, 012024 (2023).
16. Ziegler, J., Biersack, J. & Ziegler, M. SRIM–the stopping and range of ions in matter. http://www.srim.org/.
17. Khasanov, R. et al. High pressure research using muons at the Paul Scherrer Institute. *High Pressure Research* **36**, 140–166 (2016).
18. Sonier, J. E., Brewer, J. H. & Kiefl, R. F. μSR studies of the vortex state in type-II superconductors. *Rev. Mod. Phys.* **72**, 769–811 (2000).
19. Khasanov, R. et al. s-Wave Symmetry Along the c-Axis and s+d In-plane Superconductivity in Bulk $YBa_2Cu_4O_8$. *Journal of Superconductivity and Novel Magnetism* **21**, 81–85 (2008).
20. Tinkham, M. *Introduction to Superconductivity* (Dover Publications, 2004), 2 edn.
21. Prozorov, R. & Giannetta, R. W. Magnetic penetration depth in unconventional superconductors. *Superconductor Science and Technology* **19**, R41–R67 (2006).
22. Gupta, R. et al. Isotropic *s*-wave superconductivity in the noncentrosymmetric charge density wave superconductor $SrPt_2As_2$. *Phys. Rev. B* **102**, 144515 (2020).
23. Niedermayer, C., Bernhard, C., Holden, T., Kremer, R. K. & Ahn, K. Muon spin relaxation study of the magnetic penetration depth in mgb_2. *Phys. Rev. B* **65**, 094512 (2002).

24. Ding, H. et al. Observation of fermi-surface–dependent nodeless superconducting gaps in $ba_{0.6}k_{0.4}fe_2as_2$. *Europhysics Letters* **83**, 47001 (2008).
25. Szabó, P. et al. Evidence for two superconducting energy gaps in $ba_{0.6}k_{0.4}fe_2as_2$ from andreev reflection spectroscopy. *Physical Review B* **79**, 012503 (2009).
26. Yilmaz, T. et al. Orbital selective band re-normalization induced Lifshitz transition in $TiSe_2$. *Commun. Phys.* **8**, 435 (2025).
27. Moulding, O., Muramatsu, T., Sayers, C. J., Da Como, E. & Friedemann, S. Suppression of charge-density-wave order in $TiSe_2$ studied with high-pressure magnetoresistance. *Electronic Structure* **4**, 035001 (2022).
28. Koshelev, A. E. & Matveev, K. A. Anomalous density of states in multiband superconductors near the lifshitz transition. *Phys. Rev. B* **90**, 140505 (2014).
29. Hirschfeld, P., Korshunov, M. & Mazin, I. Gap symmetry and structure of fe-based superconductors. *Reports on Progress in Physics* **74**, 124508 (2011).
30. Lee, S. et al. Tuning the charge density wave quantum critical point and the appearance of superconductivity in $TiSe_2$. *Phys. Rev. Res.* **3**, 033097 (2021).
31. Marques, C. A. et al. Spin-orbit coupling induced van hove singularity in proximity to a lifshitz transition in sr4ru3o10. *npj Quantum Materials* **9**, 35 (2024).
32. Suhl, H., Matthias, B. T. & Walker, L. R. Bardeen-cooper-schrieffer theory of superconductivity in the case of overlapping bands. *Phys. Rev. Lett.* **3**, 552–554 (1959).
33. Leggett, A. J. Number-phase fluctuations in two-band superconductors. *Progress of Theoretical Physics* **36**, 901–930 (1966).
34. Mazin, I. I., Singh, D. J., Johannes, M. D. & Du, M. H. Unconventional superconductivity with a sign reversal in the order parameter of $lafeaso_{1-x}f_x$. *Phys. Rev. Lett.* **101**, 057003 (2008).
35. Joe, Y. I. et al. Emergence of charge density wave domain walls above the superconducting dome in $TiSe_2$. *Nature Phys.* **10**, 421–425 (2014).
36. van Wezel, J., Nahai-Williamson, P. & Saxena, S. S. Exciton-phonon-driven charge density wave in $tise_2$. *Phys. Rev. B* **81**, 165109 (2010).
37. Qian, D. et al. Emergence of fermi pockets in a new excitonic charge-density-wave melted superconductor. *Phys. Rev. Lett.* **98**, 117007 (2007).
38. Zhao, J. F. et al. Evolution of the electronic structure of $1t\text{-}cu_xtise_2$. *Phys. Rev. Lett.* **99**, 146401 (2007).
39. Morosan, E., Li, L., Ong, N. P. & Cava, R. J. Anisotropic properties of the layered superconductor $cu_{0.07}Tise_2$. *Phys. Rev. B* **75**, 104505 (2007).
40. Xu, S.-Y. et al. Observation of fermi arc surface states in a topological metal. *Nature Physics* **10**, 943–950 (2014).
41. Qian, X., Liu, J., Fu, L. & Li, J. Quantum spin hall effect in two-dimensional transition metal dichalcogenides. *Science* **346**, 1344–1347 (2014).
42. Sato, M. & Ando, Y. Topological superconductors: a review. *Reports on Progress in Physics* **80**, 076501 (2017).
43. Wu, Y.-M. & Wang, Y. d-wave charge-4e superconductivity from fluctuating pair density waves. *npj Quantum Materials* **9**, 66 (2024).
44. Shermadini, Z. et al. A low-background piston–cylinder-type hybrid high pressure cell for muon-spin rotation/relaxation experiments. *High Pressure Research* **37**, 449–464 (2017).
45. Khasanov, R. & Ummarino, G. A. Pressure weakens coupling strength in in and sn elemental superconductors. *Phys. Rev. B* **110**, 214515 (2024).
46. Suter, A. & Wojek, B. M. Musrfit: A free platform-independent framework for μsr data analysis. *Phys. Proc.* **30**, 69 (2012).

Acknowledgements

The μ^+SR measurements were performed at the Swiss Muon Source (SμS), at the Paul Scherrer Institute in Villigen, Switzerland. We thank the staff of PSI for help with the μ^+SR experiments. This research is funded by the Swedish Foundation for Strategic Research (SSF) within the Swedish national graduate school in neutron scattering (SwedNess), as well as the Swedish Research Council VR (Dnr. 2021-06157 and Dnr. 2022-03936), and the Carl Tryggers Foundation for Scientific Research (CTS-22:2374). Y.S. is supported by the Wallenberg Academy Fellows through the grant 2021-0150. G.S. acknowledges funding from the Chalmers X-Ray and Neutron Initiatives (CHANS) grant and European Union's Horizon 2020 research and innovation program under the Marie Skłodowska-Curie grant agreement No 884104 (PSI-FELLOW-III-3i). O.K.F is supported by the Swedish Research Council (VR) through Grant 2022-06217, the Foundation Blanceflor fellow scholarships for 2023 and 2024, and the Ruth and Nils-Erik Stenbäck Foundation. All images involving crystal structure were made with the VESTA software and the μ^+SR data was fitted using musrfit[46]. F.E. greatly acknowledges Y. Ge for their work on the resistivity measurements.

Author contributions

M.M. and Y.S. conceived the project. M. A.-H. grew the *1T*-$TiSe_2$ single crystals. The μ^+SR experiments were performed by F.E., G.S., J.P., O.K.F, D.D. and R.K. Data analysis and simulations were carried out by F.E. The manuscript was written by F.E., M.M. and Y.S. with input from all authors.

Funding

Open access funding provided by Royal Institute of Technology.

Competing interests

The authors declare no competing interests.

Additional information

Supplementary information The online version contains supplementary material available at https://doi.org/10.1038/s41535-025-00834-8.

Correspondence and requests for materials should be addressed to F. Elson, Y. Sassa or M. Månsson.